2002

Systematic first-principles study of impurity hybridization in NiAl

David Djajaputra

Bernard R. Cooper

Systematic first-principles study of impurity hybridization in NiAl

David Djajaputra and Bernard R. Cooper
Department of Physics, West Virginia University, P.O. Box 6315, Morgantown, WV 26506-6315
(June 4, 2018)

We have performed a systematic first-principles computational study of the effects of impurity atoms (boron, carbon, nitrogen, oxygen, silicon, phosporus, and sulfur) on the orbital hybridization and bonding properties in the intermetallic alloy NiAl using a full-potential linear muffin-tin orbital method. The matrix elements in momentum space were used to calculate real-space properties: onsite parameters, partial densities of states, and local charges. In impurity atoms that are empirically known to be embrittler (N and O) we found that the 2*s* orbital is bound to the impurity and therefore does not participate in the covalent bonding. In contrast, the corresponding 2*s* orbital is found to be delocalized in the cohesion enhancers (B and C). Each of these impurity atoms is found to acquire a net negative local charge in NiAl irrespective of whether they sit in the Ni or Al site. The embrittler therefore reduces the total number of electrons available for covalent bonding by removing some of the electrons from the neighboring Ni or Al atoms and localizing them at the impurity site. We show that these correlations also hold for silicon, phosporus, and sulfur.

I. INTRODUCTION

The development of better nickel-based superalloys has paced the construction of larger, more powerful, and more fuel efficient aircraft and industrial gas turbines. [1,2] Aluminum is the most important alloying element in nickel, for both strength and oxidation resistance. [1,3,4] Pure NiAl, which crystallizes in the B2 structure, has low density, high melting temperature of 1638°C (melting temperature for the fcc nickel is 1455°C), and good electrical and thermal conductivity. [4,5] Its practical application, however, is limited by poor toughness and damage tolerance at room temperature [5] and brittle grain-boundary fracture at ambient and elevated temperature. [6] The strength and other properties of NiAl can be modified by adding various impurity atoms. Typical modern nickel-base superalloys contain eight or more different elements, each with specific functions with respect to strength, alloy stability, and environmental resistance. [1] Certain elements have been found to be deleterious to the properties of NiAl, among them are nitrogen, oxygen, silicon, phosphorus, and sulfur. [1] The presence of these elements must be controlled during the melting processes. On the other hand, some other elements are desirable because they improve the cohesive properties of NiAl. Chromium impurities are important for improving its hot corrosion resistance, while boron, carbon, and zirconium provide improved resistance of grain boundaries to fracture at elevated temperatures. [1,6] Stoloff has given an extensive list of atomic additives and their effects on the properties of nickel-base superalloys. [1]

Boron is the main grain-boundary strengthener in NiAl. The beneficial effect of boron additives was first observed by Aoki and Izumi in 1979. [7] Boron has a strong tendency to segregate to grain boundaries and it can improve the tensile ductility of a polycrystal by an order of magnitude. [6] This increase in tensile ductility is accompanied by a change in the fracture mode from brittle intergranular to ductile transgranular [6] which clearly shows the effectiveness of boron in improving the intergranular cohesion in a polycrystal. The strengthening effect of boron additives has also been observed when they are present as impurity atoms in bulk. The improvement in strength obtains even with a small concentration of boron dopants: 30 weight ppm of boron can give rise to a 30% increase in yield strength. [8] In addition to boron, carbon, which is the element next to boron in the periodic table, is also a potent strengthener in NiAl. [5]

In contrast to boron and carbon, oxygen and nitrogen are known to be harmful to the cohesion in NiAl. Indeed oxidation is among the most common degradation mechanisms in many metals and alloys. [9,10] In NiAl, oxygen will selectively attack the least noble constituent, which is aluminum, and form the stable oxide product Al_2O_3. [11] The rate of formation of NiO is negligible compared to that of Al_2O_3. [4,6,11] This strongly-preferential bonding has also been shown to occur in some recent first-principles calculations [12,13] and it may be among the key microscopic ingredients for the formation of various mesoscopic structures (e.g., pores, cracks, and blisters) created during an oxygen attack on an intermetallic alloy. [9] In the extreme, oxygen can cause the pesting degradation phenomenon which happens when some polycrystalline samples are heated in air within a certain range of intermediate to high temperatures. [10,11] This process, which is essentially a spontaneous disintegration of the polycrystalline alloy to powder, can take place in a matter of several hours. [14,15]

There have been several first-principles calculations in the literature on the effects of impurities on the cohesion in nickel aluminides and related alloys. Sun *et al.* have studied the effects of boron and hydrogen on Ni_3Al using a full-potential linear muffin-tin orbital (FPLMTO) method. [16] They emphasized the increase of the inter-

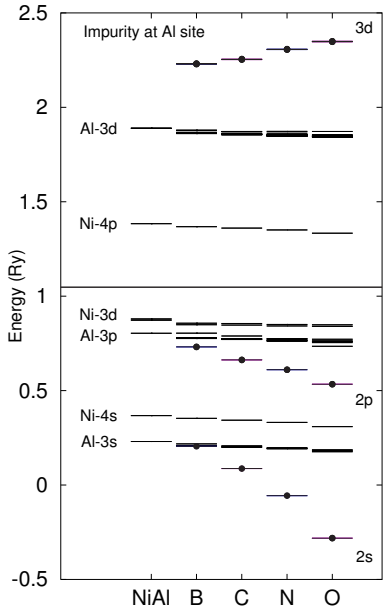

FIG. 1. Onsite parameters for orbitals in 16-atom supercells of NiAl with one impurity atom substituting for Al. The leftmost column gives the onsite parameters for pure NiAl. The lines with dots are the onsite parameters for the $2s$, $2p$, and $3d$ orbitals at the impurity atom. The horizontal line at $E_F = 1.0475$ Ry is the Fermi level of the pure NiAl. The Fermi energy for the supercell is 1.0105, 1.0085, 0.9943, and 0.9927 Ry for B, C, N, and O, respectively.

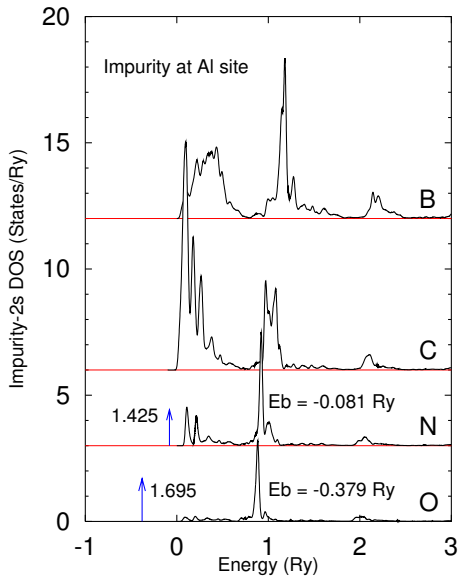

FIG. 2. Site-projected $2s$ density of states at the impurity atom for the case where it is substituting an Al atom. Notice the strong resonance at the bottom of the band in the case of carbon. The delta functions shown in the spectra for N and O are actually very narrow bands (in our supercell calculation) with bandwidth of 0.0226 Ry and 0.00198 Ry, respectively. The numbers next to the arrows are the partial weights of the impurity $2s$ state in the band, while E_b denotes the center of the band. The Fermi level of NiAl is at $E_F = 1.0475$ Ry. Each spectrum has been given a separate vertical shift for clarity.

stitial bonding charge as the origin of the beneficial effect of boron. Wu *et al.* calculated the effects of boron and phosphorus on the grain-boundary cohesion of iron using a full-potential linear augmented plane-wave (FPLAPW) method. [17] They showed that a combination method of the thermodynamic theory of Rice and Wang [18,19] and first-principles total-energy calculations can be used to determine the grain-boundary embrittlement potency of a given impurity. Using the same combination method they have also studied the effects of hydrogen and carbon impurities in iron and hydrogen, boron, and phosporus in nickel. [20–22] Vacancies and antistructure defects in transition-metal aluminides have been studied by several different groups. [23–25]

Previous first-principles studies on the effects of impurity atoms in nickel aluminides have generally focused on, and drawn their conclusions from, the calculated total energy and electronic charge densities. Insights into the bonding and hybridization in the system, however, can usually be obtained more clearly by working with localized basis functions and using the simpler tight-binding representation. [26–28] Recently we have shown that accurate tight-binding parameters can be obtained directly from the FPLMTO method. [29] In this paper we have used this method to perform a systematic study of impurities on NiAl. The motivation for carrying out a systematic study is the widely different effects that can be caused by "nearby" atoms in the periodic table. It is not obvious, e.g., why, along the $2p$ row, boron and carbon are good cohesion enhancers in NiAl while the next elements, nitrogen and oxygen, are embrittlers. The present study has been carried out in an effort to find the answer to this question. In the next section, we will give a brief description of the FPLMTO method that we use. The rest of the paper presents the results of our calculations.

II. FPLMTO METHOD

We use the Wills-Price all-electron full-potential implementation of the LMTO method. [30–32] In FPLMTO, no assumption is made about the form of the wave functions, charge density, or potential. The muffin-tin potential is used only to construct the LMTO basis functions but the final wave functions, and other quantities derived from them, are not limited to such form. [29] Relativistic Dirac equations are used for the core states, while the valence states are treated semirelativistically without spin-orbit coupling. For the exchange-correlation potential, we use the parametrization of Vosko, Wilk, and Nusair. [33] Within the muffin-tin spheres, lattice harmonics with angular momentum $l \leq 8$ are used. NiAl is a good paramagnetic metal (it has no measurable magnetic ordering down to temperatures of a few Kelvin [34,35]) therefore we do not use spin polarization in our calculation.

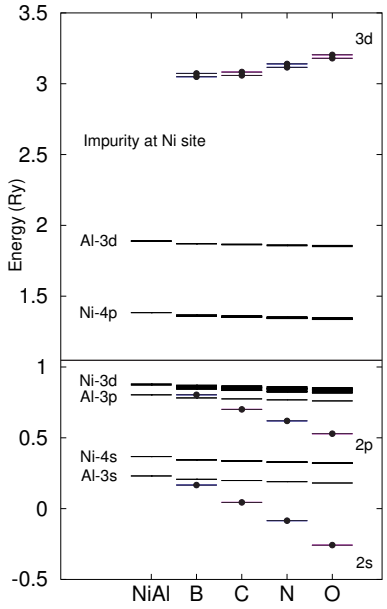

FIG. 3. Onsite parameters for orbitals in 16-atom supercells of NiAl with one impurity atom substituting for Ni. The leftmost column gives the onsite parameters for pure NiAl. The lines with dots are the onsite parameters for the $2s$, $2p$, and $3d$ orbitals at the impurity atom. The horizontal line at $E_F = 1.0475$ Ry is the Fermi level of the pure NiAl. The Fermi energy for the supercell is 1.0283, 1.0185, 1.0051, and 1.0014 Ry for B, C, N, and O, respectively.

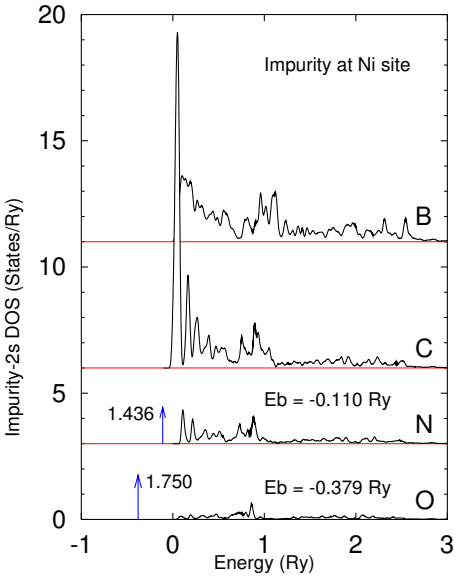

FIG. 4. Site-projected $2s$ density of states at the impurity atom for the case where it is substituting a Ni atom. Notice the strong resonance at the bottom of the band in the case of carbon. The delta functions shown in the spectra for N and O are actually very narrow bands (in our supercell calculation) with bandwidth of 0.0225 Ry and 0.00158 Ry, respectively. The numbers next to the arrows are the partial weights of the impurity $2s$ state in the band, while E_b denotes the center of the band. The Fermi level of NiAl is at $E_F = 1.0475$ Ry. Each spectrum has been given a separate vertical shift for clarity.

Impurity is incorporated in our FPLMTO calculations by using a 16-atom supercell. [13] NiAl crystallizes in B2 structure which is a bcc-based structure with one atom (Ni or Al) occupying the center of the cube $(\frac{1}{2},\frac{1}{2},\frac{1}{2})$ and the other (Al or Ni) at the corner of the cube $(0,0,0)$. The cubic supercell is constructed from 2^3 NiAl unit cells and the impurity atom is placed at the center of the supercell. Each atom is assigned a minimal basis set consisting of 9 (spd) orbitals. Since we want to work with localized orbitals, the interstitial parameter for each orbital has been uniformly set at $\kappa = -0.2$ a.u. This gives well-localized FPLMTO basis functions with an envelope that decays roughly as $\exp(-|\kappa|r)$. [29]

The standard FPLMTO method self-consistently calculates the basis functions, along with the corresponding charge density and the resulting total energy, by working in momentum space. The program computes the matrix elements of the hamiltonian, $H_{\alpha\beta}(\mathbf{k})$, and the overlap, $S_{\alpha\beta}(\mathbf{k})$, matrices from which the energy bands $\varepsilon(\mathbf{k})$ are obtained by diagonalization. From these matrix elements in momentum space, we have calculated the matrix elements in real space by direct Fourier transform:

$$H_{\alpha\beta}(\mathbf{k}) = \sum_j \exp\left(i\mathbf{k}\cdot\mathbf{R}_j\right) H_{\alpha\beta}(\mathbf{R}_j). \qquad (1)$$

The onsite parameters are simply the hamiltonian matrix elements, in real space, between identical orbitals, $H_{\alpha\alpha}(\mathbf{R}=\mathbf{0})$. This is computed by using an additional code built on top of our FPLMTO program. The distribution of onsite parameters is an important ingredient in, e.g., Anderson's theory of diagonal localization. [36–39] In this theory, the distribution of onsite parameters, characterized by the width of the distribution W, competes with the strength of the hybridization between the orbitals, which in the impurity case can be taken to be the bandwidth of the parent system B. Electron localization is more favorable for large values of W/B. [37]

To obtain a measure of the hybridization strength between the orbitals in the system, without having to deal explicitly with the multiplicity of hopping and overlap parameters, one can instead examine the density of states (DOS) and its atomic-site and angular-momentum projections. [40–42] Spin projection is unnecessary since NiAl is paramagnetic and we do not use spin polarization in our calculations. In this paper the total DOS and its projections have been computed using the standard tetrahedron method with 35 points in the irreducible wedge of the cubic Brillouin zone. The total DOS is calculated by summing the contributions from all bands and all tetrahedra: [43]

$$\rho(E) = \sum_{n,\mathbf{k}_c} g_n(\mathbf{k}_c; E), \qquad (2)$$

where n is the band index while $\mathbf{k}_c$ is the index for the tetrahedra. The site (index i) and angular-momentum

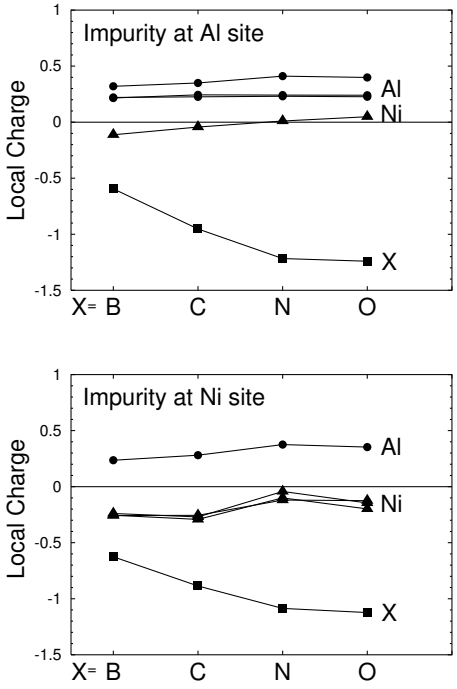

FIG. 5. Local charge (in units of the electron charge $|e|$) induced on each atom in the supercell for the case where an impurity atom (X = B, C, N, and O) is substitutionally placed at an Al site (top panel) and a Ni site (bottom panel). Aluminum charges are marked by filled circles (•), Ni by filled triangles, while the impurity charges are shown as filled squares. In pure NiAl, Al has a charge of +0.2 while, from charge neutrality, Ni has the opposite charge of −0.2.

(index l) projection of the DOS is obtained by multiplying each contribution with its decomposition weight $w_{nil}(\mathbf{k}_c)$ which is obtained from the wavefunctions:

$$\rho_{il}(E) = \sum_{n,\mathbf{k}_c} w_{nil}(\mathbf{k}_c) \cdot g_n(\mathbf{k}_c; E). \tag{3}$$

Standard DOS decomposition in the FPLMTO method differentiates between the muffin-tin (MT) and the interstitial components of the electron distribution. [16] Further site and angular-momentum decomposition, i.e. the calculation of the weights $w_{nil}(\mathbf{k}_c)$, is then performed *only* on the part of the LMTO wavefunction *inside* the MT spheres. The interstitial part is not considered to belong to any particular site and therefore is not subjected to further decomposition. It should be noted that this differentiation between MT and interstitial charge is an artificial one since it depends on the size of the MT sphere which, in common practice, is set rather arbitrarily by the user of the FPLMTO code. Furthermore, the interpretation of such a decomposition is difficult since, e.g., the integrated spectral weight for a particular atom (v_i) is, in general, less than the total number of valence electrons assigned to it (n_i):

$$v_i^{(\mathrm{LMTO})} = \sum_{l=0}^{l_m} \int_{-\infty}^{\infty} \rho_{il}^{(\mathrm{LMTO})}(E)\, dE \;\le\; n_i. \tag{4}$$

Note that the summation over the angular momenta extends up to l_m, which is a free parameter in an FPLMTO calculation (this parameter is set to 8 in this work). In general, this parameter is different from (usually much greater than) the highest angular momentum L_m that one uses in defining the FPLMTO basis functions (L_m = 2 for *spd* basis that we use here). Inside each MT, tails from the basis functions centered at other MTs give rise to higher angular-momentum harmonics when expanded relative to the center of the MT sphere. The parameter l_m is the cutoff value used in this expansion. [29]

Instead of using this MT decomposition, in this paper we have chosen to use an orthogonal decomposition which is the one used in tight-binding systems. The FPLMTO non-orthogonal matrix elements, $H_{\alpha\beta}(\mathbf{k})$ and $S_{\alpha\beta}(\mathbf{k})$, are first transformed into an orthogonal system by Löwdin transformation. [44] Since this is a symmetry transformation which does not mix components of different angular momenta, [45,46] the weights for the l-projected DOS can be obtained readily from the resulting Löwdin eigenvectors. Details on this scheme have been presented in an earlier paper. [29] In this decomposition, the angular momentum expansion extends only to L_m and the total atomic weight is equal to the number of the assigned valence electrons since the interstitial continuation of each FPLMTO basis function has been incorporated properly:

$$v_i^{(\mathrm{TB})} = \sum_{l=0}^{L_m} \int_{-\infty}^{\infty} \rho_{il}^{(\mathrm{TB})}(E)\, dE = n_i. \tag{5}$$

This decomposition method is more appropriate to use in our case since we exclusively use localized FPLMTO basis functions (specified by negative κ parameter). It should be pointed out that the Löwdin transformation to orthogonal system is used solely to obtain the decomposition weight $w_{nil}(\mathbf{k}_c)$ for the local DOS; elsewhere in this paper we work directly with *non*-orthogonal TB systems. The onsite parameters displayed in Figs. 1 and 3, e.g., are matrix elements of the hamiltonian operator in the original non-orthogonal FPLMTO basis; they are not, and should not be confused with, the matrix elements in a Löwdin orthogonal basis which are nowhere presented or analyzed in this paper.

From the projected DOS, the total number of electrons residing on each atomic site can be obtained by integrating the corresponding DOS up to the Fermi energy:

$$q_i = \sum_{l=0}^{L_m} \int_{-\infty}^{E_F} \rho_{il}(E)\, dE. \tag{6}$$

Here E_F is the self-consistent Fermi energy calculated for each supercell (with impurity atom) and not the Fermi

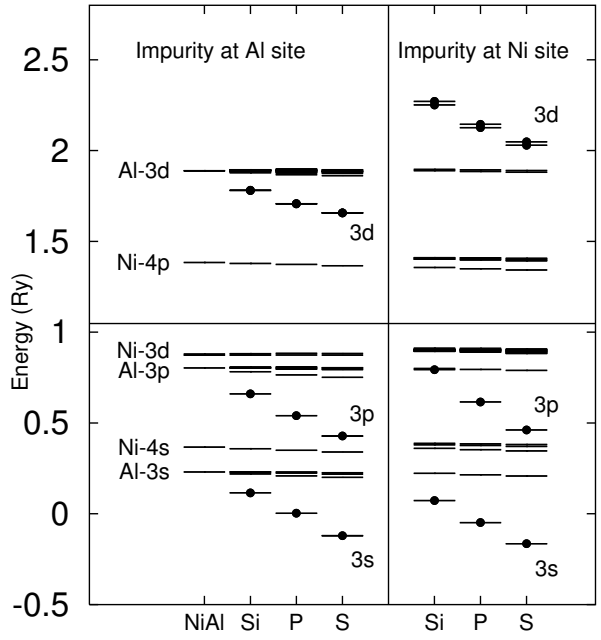

FIG. 6. Onsite parameters for orbitals in 16-atom supercells of NiAl with one impurity atom (Si, P, or S) substituting for Al (on the left side of the vertical midline); and with the impurity substituting for Ni (right side). The leftmost column gives the onsite parameters for pure NiAl. The lines with dots are the onsite parameters for the $3s$, $3p$, and $3d$ orbitals at the impurity atom. The horizontal line at $E_F = 1.0475$ Ry is the Fermi level of the pure NiAl. In the case where the impurity is occupying an Al site, the Fermi energy for the supercell is 1.0440, 1.0465, and 1.0426 for Si, P, and S, respectively. For the case where it is occupying a Ni site, the Fermi energies are 1.0765 Ry (Si), 1.0795 Ry (P), and 1.0750 Ry (S).

energy of the pure NiAl system. In the next section, we present the results of our calculations for the onsite parameters, projected DOS, and the local charges.

III. COMPUTATIONAL RESULTS

A. Boron, Carbon, Nitrogen, and Oxygen

Fig. 1 displays the calculated onsite parameters in pure NiAl and in 16-atom supercells of NiAl with one impurity atom substituting for Al. We have used the *computed* equilibrium lattice constant for NiAl (5.3451 a.u.) which is within 2% of the experimental value (5.4450 a.u.). The XAl_7Ni_8 supercell (here X stands for the impurity atom) is constructed from 2^3 NiAl unit cells [13] with the impurity atom placed at $(0,0,0)$; Al atoms at $(\frac{1}{2},0,0)$, $(\frac{1}{2},\frac{1}{2},0)$, $(\frac{1}{2},\frac{1}{2},\frac{1}{2})$, and other equivalent positions obtained by permuting the x, y, z coordinates; and Ni atoms at $(\pm\frac{1}{4},\pm\frac{1}{4},\pm\frac{1}{4})$ (in units of supercell lattice constant). Note that the positions of the Ni atoms are all symmetry-equivalent in this supercell. Al atoms, on the other hand, occupy three inequivalent sites. This gives rise to a small splitting of the Al onsite parameters as can be seen in Fig. 1; the corresponding splitting of the Ni parameters in the XNi_7Al_8 supercell can be seen in Fig. 3. Atomic relaxation has been shown to produce only a small change in energy [13] and therefore has been ignored in this work. The small value of the computed relaxation energy, [13] and the small size of the onsite-parameter splittings in Figs. 1 and 3, provide the justification for our neglect of atomic relaxation in the present work. It is unlikely that relaxation will make large quantitative change in, or rearrange the qualitative structure of, the onsite-parameter maps in Figs. 1 and 3 on which we will base much of our discussion in this paper.

The utility of plotting the onsite parameters systematically, as in Fig. 1, comes from the fact that it shows clearly how well the $2s$ and $2p$ parameters of boron match those of the corresponding $3s$ and $3p$ orbitals of aluminum, and how rapidly this compatibility deteriorates as we go from boron to oxygen. To our knowledge this almost-perfect compatibility has never been pointed out previously in the literature. The onsite parameters for the $3d$ states of the impurity atoms are all much higher than the Al-$3d$ parameters. Although results from the local density approximation (LDA) for the excited states are known in general to be less accurate than the corresponding results for the occupied states, we believe this visible difference is an important feature in explaining the efficacy of boron as a cohesion enhancer in NiAl. The much higher B-$3d$ parameters would allow the delocalized B-$2s$ and B-$2p$ states to create wider bands centered at their corresponding onsite parameters which, as we pointed out previously, match closely to those of Al-$3s$ and Al-$3p$. The overall cohesion is therefore improved by increasing the bond order (the difference in occupancy between bonding and antibonding states). [47]

The bottom of the pure-NiAl bands lies just above the zero energy in Fig. 1. It can therefore be seen clearly that the C-$2s$ onsite parameter sits just above this bottom while those of N-$2s$ and O-$2s$ orbitals lie below the main manifold of pure NiAl. As in standard scattering theory, [48] this situation opens the possibility for the existence of resonance or bound states. In Fig. 2 we show the $2s$ projected DOS at the impurity atoms. The total weight under each curve is equal to 2 (due to spin sum) to within 2% accuracy. For this case, where the impurity atom is occupying an Al site, the nearest neighbors of the impurity atom are Ni atoms. The main feature of the DOS for B-$2s$ is a broad band which is cleaved by its interaction with the neighboring $3d$ orbitals of Ni. [48,49] This is markedly different from the DOS for C-$2s$ in which the dominating feature is the strong resonant peak at the bottom of the spectrum. As we move on to N-$2s$ and O-$2s$, the onsite parameters for these orbitals are deep enough to localize the electrons in a bound state. This results in a transfer of the spectral weight from the

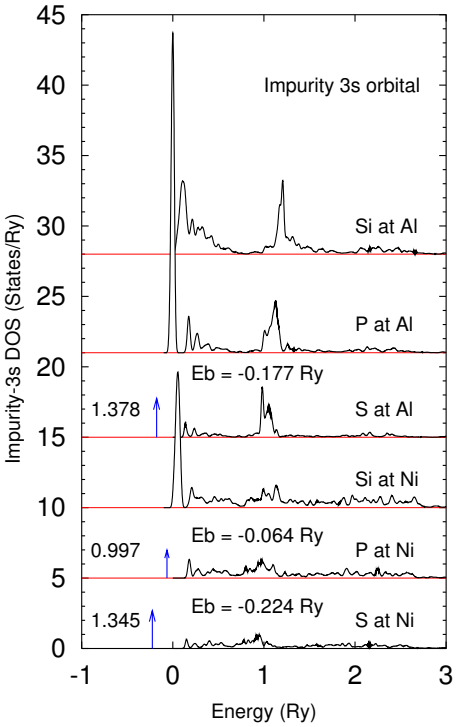

FIG. 7. Site-projected 3s density of states at the impurity site (Si, P, or S). A bound state is formed for the cases of phosporus atom at Ni site and sulfur atom at Al or Ni site. The delta functions shown in the spectra are actually very narrow bands (in our supercell calculation) with a bandwidth of 47 mRy (P at Ni), 26 mRy (S at Al), and 16 mRy (S at Ni). The numbers next to the arrows are the partial weights of the impurity 3s state in the corresponding narrow band, while E_b denotes the center of the band. The Fermi level of NiAl is at $E_F = 1.0475$ Ry. Each spectrum has been given a separate vertical shift for clarity.

continuum to the bound state. In our supercell calculation, the bound state is not manifested as a true delta function but it rather appears as a very narrow band (with bandwidth of 23 mRy and 2 mRy for N-2s and O-2s, respectively, for the case where the impurity is placed at an Al site) which is separated by a gap from the main spectrum and is displayed as a vertical arrow in Fig. 2. This narrow band still contains small hybridization components from other orbitals (this, of course, is just an artifact of a supercell calculation) which, as expected, diminish as we go from N to O. The total weight of the impurity-2s state in the narrow band is displayed next to its arrow in Fig. 2 while the rest of the weight still remains spread out thinly in the continuum.

A very similar map of onsite parameters is obtained in the alternative case where the impurity atom is substituting for a Ni atom, as shown in Fig. 3. The main difference from Fig. 1 is the fact that the impurity-3d levels are pushed to much higher values in this case (by about $0.7 - 0.8$ Ry). This feature is mainly due to the smaller size of Ni, compared to Al, which increases the kinetic energy of the orbital (we use a MT radius of 2.30 a.u. for Al and 1.85 a.u. for Ni). Combined with the bond-order argument described previously, this also provides a heuristic explanation on why an oxygen impurity would prefer to occupy a nickel site over an aluminum site, a result which was recently obtained from a full-fledged FPLMTO calculation. [13] The calculated impurity-2s DOS for the case of impurity at Ni site is shown in Fig. 4. The general progression from B to O is the same as in Fig. 2: A broad band for B-2s, strong resonance for C-2s, and bound state with an increasing binding energy for N-2s and O-2s. Since the impurity atom is surrounded by Al nearest neighbors in this case, instead of Ni atoms, we do not see as strong a band cleavage around the energy of the Ni-3d orbitals as seen in Fig. 2. Below the Fermi energy, the similarity of the results obtained for impurity at Al and Ni sites shows that these features, e.g. the compatibility of the onsite parameters for B and Al in NiAl environment, are largely independent of the atomic arrangement in the crystal. This is not surprising since an onsite parameter is sensitive only to the average potential at its atomic site. This suggests that our results in this paper, which have been obtained for NiAl host using 16-atom supercells, may have some relevance also to other nickel-aluminide alloys with different concentrations of impurity atoms.

Fig. 5 shows the charges induced on each atom in the supercell which have been calculated by substracting the total number of electrons on the site, q_i in Eq.(6), from the assigned number of valence electrons n_i:

$$Q_i = n_i - q_i. \tag{7}$$

In all cases, Ni is found to be more electronegative than Al (the Pauling electronegativity of Ni and Al is 1.91 and 1.61 respectively [50]). In pure NiAl, Al has a charge of $+0.2$ (in units of electron charge $|e|$) while, from charge neutrality, Ni has the opposite charge of -0.2. The impurities from the 2p row that we have studied in this work have Pauling electronegativity of 2.04, 2.55, 3.04, and 3.44 for B, C, N, and O, respectively. [50] It can be seen that this electronegativity trend is followed rather well in Fig. 5. In the case of impurity atom at Al site (top panel in Fig. 5), N and O are sufficiently electronegative to change the sign of the induced charge on their Ni nearest neighbors, relative to the sign of the corresponding charge when B or C is present. Thus a portion of the valence electrons localized at the N or O bound state comes from their nearest-neighbor Ni atoms. In the alternative case where the impurity is occupying the Ni site, a jump in the induced charge on the Ni atoms is clearly seen in the bottom panel of Fig. 5. Although in this case they are no longer the nearest neighbors of the impurity (since they are separated from it by the Al atoms), the formation of the bound state in N and O still has a substantial effect on the Ni atoms. Two reasons may be

given to explain this strong interaction between the impurity and the Ni atoms. First, the Al nearest neighbors are already positively charged, therefore it is relatively harder for the impurity atom to attract their electrons. Second, the DOS of NiAl is dominated by strong Ni-3d peaks which are situated just below the Fermi energy. [13] These peaks are sufficiently wide to suggest that the Ni-3d electrons in this alloy are well delocalized. Their proximity to the Fermi energy then strongly expose them to changes in the potential as that caused by the formation of a bound state on a nearby atom.

B. Silicon, Phosphorus, and Sulfur

The elements from the 3p row of the periodic table: Si, P, and S, have been known to be strong embrittlers in NiAl. [1] It is therefore interesting to examine whether the correlation that we have obtained in the previous subsection between the matching of the onsite parameters and the macroscopic embrittling/strengthening potency of the impurity persists also for these elements. Fig. 6 displays the calculated onsite parameters for orbitals in 16-atom supercells of NiAl containing one impurity atom (Si, P, or S) which substitutes for an Al (shown on the left side of the vertical midline in Fig. 6) or a Ni atom (shown on the right side of the midline). A major difference from the corresponding plots of onsite parameters in Fig. 1 and Fig. 3 is the decreasing trend of the impurity-3d levels as we go to higher atomic number (from Si to S). This is due to the fact that the basis orbitals that we use in this case (3s, 3p, and 3d) all have the same principal quantum number. The difference in their levels therefore originates mainly from the difference in the effective centrifugal potential (the $l(l+1)r^{-2}$ term in the radial Schrödinger equation), which is independent of the atomic number. [51,52] In contrast, the basis orbitals that we use for the 2p elements in Fig. 1 and Fig. 3 (2s, 2p, and 3d) come from two different principal quantum number shells. In this case, in addition to the centrifugal potential, the splitting among the onsite levels is also determined by the Coulomb potential of the nucleus which increases with the atomic number. Thus the 2p level decreases in concert with the 2s level while the splitting between them and the 3d level increases with the atomic number as we go from boron to oxygen in Figs. 1 and 3.

Fig. 7 shows the resulting projected DOS for the lowest-lying valence (3s) state of Si, P, and S at the impurity site. As in Fig. 2, when the impurity is placed at the Al site, its DOS features a peak close to the Fermi energy due to its strong hybridization with the 3d states of its neighboring Ni atoms. Except for the case of Si at Al site, where the resonance at the bottom of the spectrum is relatively weak, the DOS curves in Fig. 7 are all dominated either by a very strong resonance (P at Al; Si at Ni) or a bound state that is completely separated from the main spectrum (S at Al; P at Ni; and S at Ni). Silicon, phosporus, and sulfur are known to be embrittlers in NiAl. [1] These results therefore support the correlation that we have obtained in the previous section that relates the localization of the valence electrons at the impurity site with the macroscopic embrittling character of the impurity atom when it is present in NiAl.

Although the weak resonance in the case of Si at Al site seems to defy this correlation (note that, for reason of presentation clarity, the projected-DOS curves that we show in Figs. 2, 4, and 7 have been obtained by convoluting the FPLMTO DOS with a Gaussian smearing function of width about 10 mRy), it should also be noted that its 3d-state level in Fig. 6 is much lower than the corresponding 3d level for, e.g., boron or carbon in Fig. 1. As has been pointed out in the previous subsection, this much-lower 3d level exerts an 'onsite pressure' on its lower-lying s and p states against forming a wider band (due to its orthogonality with these states). This results in narrower bands under the Fermi level and, consequently, in reduced bond order and weaker metallic character of bonding around the impurity site. This may explain why silicon is an embrittler in NiAl while carbon, which has a similar set of onsite parameters below the Fermi energy as can be seen by comparing Fig. 1 and Fig. 6, is in contrast a cohesion enhancer.

IV. SUMMARY

In this paper we have performed a systematic study of impurity hybridization in the refractory alloy NiAl. Impurity atoms from the 2p row (B, C, N, and O) and the 3p row (Si, P, and S) of the periodic table have been examined. The purpose of this study is to understand the origin of the embrittling/strengthening property of impurity atoms in alloys in terms of the compatibility of their onsite parameters and their orbital hybridization. We found that the onsite parameters of boron, which is the prime cohesion enhancer in NiAl, are highly compatible with those of the NiAl host below the Fermi energy. In addition, its higher-lying atomic levels are located higher than the corresponding levels for Al. This allows the 2s and 2p states of boron to hybridize more strongly with the orbitals at the neighboring atoms, form wider valence bands centered below the Fermi energy, and increase the bond order. These two properties, the compatibility of the onsite parameters and the relative location of the higher-lying states of the impurity atom, have been found useful in understanding the electronic structure of the impurities and their effects on the cohesion in NiAl.

It is a pleasure to thank Dr. Leonid Muratov for many stimulating discussions and useful inputs. This work was supported by AF-OSR Grant No. F49620-99-1-0274.

[1] N.S. Stoloff, in *Microstructure and Properties of Materials, Vol. 1*, edited by J.C.M. Li (World Scientific, Singapore, 1996), pp. 51–106.

[2] R. Darolia, JOM **43**, 44 (1991).

[3] C.P. Blankenship Jr., E.A. Starke Jr., and E. Hornbogen, in *Microstructure and Properties of Materials, Vol. 1*, edited by J.C.M. Li (World Scientific, Singapore, 1996), pp. 1–50.

[4] D.B. Miracle, Acta Metall. Mater. **41**, 649 (1993).

[5] D.B. Miracle and R. Darolia, in *Intermetallic Compounds: Principles and Practice, Vol. 2—Practice*, edited by J.H. Westbrook and R.L. Fleischer (John Wiley and Sons, Chichester, England, 1995), pp. 53–72.

[6] C.T. Liu and E.P. George, in *International Symposium on Nickel and Iron Aluminides: Processing, Properties, and Applications*, edited by S.C. Deevi *et al.* (ASM International, Materials Park, OH, 1997), pp. 21–31.

[7] K. Aoki and O. Izumi, Nippon Kinzoku Gakkaishi **43**, 1190 (1979).

[8] E.P. George, C.T. Liu, and J.J. Liao, in *Alloy Phase Stability and Design*, edited by G.M. Stocks, A.F. Giamei, and D.P. Pope (MRS Proc. **186**, 1990), p. 186.

[9] O. Kubaschewski, B.E. Hopkins, *Oxidation of Metals and Alloys*, Academic Press, London, 1962.

[10] J. Doychak, in *Intermetallic Compounds: Principles and Practice, Vol. 1—Principles*, edited by J.H. Westbrook and R.L. Fleischer (John Wiley and Sons, Chichester, England, 1995), pp. 977–1016.

[11] E.A. Aitken, in *Intermetallic Compounds*, edited by J.H. Westbrook (John Wiley and Sons, New York, 1966), pp. 491–516.

[12] A.Y. Lozovoi, A. Alavi, and M.W. Finnis, Phys. Rev. Lett. **85**, 610 (2000).

[13] D. Djajaputra and B.R. Cooper, Phys. Rev. B **64**, 085121 (2001).

[14] T.H. Chuang, Y.C. Pan, and S.C. Hsu, Metall. Trans. A **22**, 1801 (1990).

[15] J.H. Westbrook and D.L. Wood, J. Nucl. Materials **12**, 208 (1964).

[16] S.N. Sun, N. Kioussis, S.P. Lim, A. Gonis, and W.H. Gourdin, Phys. Rev. B **52**, 14421 (1995).

[17] R. Wu, A.J. Freeman, and G.B. Olson, Science **265**, 376 (1994).

[18] J.R. Rice and J.-S. Wang, Mater. Sci. Eng. A **107**, 23 (1989).

[19] P.M. Anderson, J.-S. Wang, and J.R. Rice, in *Innovations in Ultrahigh-Strength Steel Technology*, edited by G.B. Olson, M. Azrin, and E.S. Wright (Proceedings of the 34th Sagamore Army Materials Research Conference, Government Printing Office, Washington DC, 1990), p. 619.

[20] R. Wu, A.J. Freeman, and G.B. Olson, Phys. Rev. B **53**, 7504 (1996).

[21] W.T. Geng, A.J. Freeman, R. Wu, C.B. Geller, and J.E. Raynolds, Phys. Rev. B **60**, 7149 (1999).

[22] L. Zhong, R. Wu, A.J. Freeman, and G.B. Olson, Phys. Rev. B **62**, 13938 (2000).

[23] C.L. Fu, Phys. Rev. B **52**, 3151 (1995).

[24] G. Bester, B. Meyer, M. Fähnle, Phys. Rev. B **60**, 14492 (1999).

[25] M. Rasamny, M. Weinert, G.W. Fernando, and R.E. Watson, Phys. Rev. B **64**, 144107 (2001).

[26] C. Colinet, A. Bessoud, and A. Pasturel, J. Phys.: Condens. Matter **1**, 5837 (1989).

[27] D.A. Muller, P.E. Batson, and J. Silcox, Phys. Rev. B **58**, 11970 (1998).

[28] D.A. Pankhurst, G.A. Botton, and C.J. Humphreys, Phys. Rev. B **63**, 205117 (2001).

[29] D. Djajaputra and B.R. Cooper, preprint available at http://xxx.arXiv.org as cond-mat/0205368.

[30] J.M. Wills, O. Eriksson, M. Alouani, and D.L. Price, in *Electronic Structure and Physical Properties of Solids*, edited by H. Dreyssé (Springer-Verlag, Berlin, 2000), pp. 148–167.

[31] D.L. Price and B.R. Cooper, Phys. Rev. B **39**, 4945 (1989).

[32] D.L. Price, J.M. Wills, and B.R. Cooper, Phys. Rev. B **46**, 11368 (1992).

[33] S.H. Vosko, L. Wilk, and M. Nusair, Can. J. Phys. **58**, 1200 (1980).

[34] J.R. Willhite, L.B. Welsh, T. Yoshitomi, and J.O. Brittain, Solid State Commun. **13**, 1907 (1973).

[35] N.I. Kulikov, A.V. Postnikov, G. Borstel, and J. Braun, Phys. Rev. B **59**, 6824 (1999).

[36] P.W. Anderson, Phys. Rev. B **109**, 1492 (1958).

[37] J.M. Ziman, *Models of Disorder*, Cambridge University Press, Cambridge, UK, 1979.

[38] N.F. Mott, *Metal-Insulator Transitions*, Taylor and Francis, London, 1990.

[39] B.Y. Tong, M.M. Pant, and B. Hede, J. Phys. C **13**, 1221 (1980).

[40] C.M. Varma and A.J. Wilson, Phys. Rev. B **22**, 3795 (1980).

[41] A.J. Wilson and C.M. Varma, Phys. Rev. B **22**, 3805 (1980).

[42] S.M. Dunaevskii, Sov. Phys. Solid State **24**, 2110 (1980).

[43] G. Gilat, in *Methods in Computational Physics*, Vol. **15**, edited by B. Alder, S. Fernbach, and M. Rotenberg (Academic Press, New York, 1976), pp. 317–370.

[44] P.O. Löwdin, Adv. in Physics **5**, 1 (1956).

[45] J.C. Slater and G.F. Koster, Phys. Rev. **94**, 1498 (1954).

[46] S.L. Altmann, *Band Theory of Solids*, Clarendon Press, Oxford, UK, 1995.

[47] A.P. Sutton, *Electronic Structure of Materials*, Clarendon Press, Oxford, UK, 1996.

[48] E.N. Economou, *Green's Functions in Quantum Physics*, Springer-Verlag, Berlin, 1979. See Sec. 6.2.1 and Fig. 6.3.

[49] C. Sanchez-Castro, K.S. Bedell, and B.R. Cooper, Phys. Rev. B **47**, 6879 (1993).

[50] J. Emsley, *The Elements*, Clarendon Press, Oxford, UK, 1994.

[51] G.K. Woodgate, *Elementary Atomic Structure*, Clarendon Press, Oxford, UK, 1989.

[52] C.P. Flynn, *Point Defects and Diffusion*, Clarendon Press, Oxford, UK, 1972.